



Realization of high-pressure dry methane reforming by suppressing coke deposition with Co-Rh intermetallic clusters

Qing Liu ^{a,1}, Yang Liu ^{b,1}, Ning Zhou ^{a,1}, Penghao Zhang ^a, Zhicheng Liu ^c, Evgeny I. Vovk ^b,
Yi-An Zhu ^{a,*}, Yong Yang ^{b,*}, Kake Zhu ^{a,*}

^a UNILAB, State Key Laboratory of Chemical Engineering, School of Chemical Engineering, East China University of Science and Technology, Shanghai 200237, PR China

^b School of Physical Science and Technology, ShanghaiTech University, Shanghai 201203, PR China

^c Shanghai Research Institute of Petrochemical Technology, Shanghai 201208, PR China



ARTICLE INFO

Keywords:

Methane dry reforming
Carbon dioxide
Co-Rh alloy
Heterogeneous catalysis
Kinetics

ABSTRACT

It is economical to perform methane and carbon dioxide reforming under high-pressure and temperature conditions, but the harsh operation condition poses a grand challenge for coke-resistant catalyst design. We report herein that surface-segregation-free Co_1Rh_3 clusters are stable catalysts under 20 bars at 850 °C. Microkinetic analysis discloses that balanced and lowered surface coverages of C^* and O^* constitute the most abundant reaction intermediates on Co_1Rh_3 clusters at elevated pressures, with respect to that of the monometallic ones, thus avoiding surface carbon accumulation or surface oxidative deactivation. Moreover, density functional theory calculations of carbon atom nucleation disclose that adsorbed carbon transformation to refractory, graphenelike carbon is suppressed on Co_1Rh_3 cluster surface, owing to increased energetic barrier and ensemble size, hence, only CO_2 gasifiable soft carbon could form. The revelation of the electronic/geometric features of Co_1Rh_3 is regarded to provide a guidance for future coke-resistant catalyst design.

1. Introduction

Methane reforming with carbon dioxide (methane dry reforming, DRM) co-converts two green-house gases into syngas (a mixture of H_2 and CO), a versatile feedstock for the production of methanol, fuels (through Fischer-Tropsch process), dimethyl ether, high alcohols, hydroformylation product, ammonia, etc., and is regarded as a promising technology within the framework of carbon capture, utilization and storage [1,2]. Most current DRM catalyst studies are conducted under ambient pressures, which, nonetheless, are considered capital intensive for the low pressures, since methane is stored and the product syngas is consumed in downstream uses at elevated pressures (10–40 bars). It is therefore more economical to carry out the reaction under industrially relevant, pressurized conditions [3,4]. At elevated pressures, high throughput DRM conversion could be achieved and the expensive compression unit operation could be avoided or minimized, hence, significantly reducing process costs. The increase in reaction pressure, however, poses critical challenges to catalytic material and process design, because: (i) coke deposition is thermodynamically

favored under high-pressure conditions (Fig. S1, Electronic Supplementary Information, ESI); (ii) increase in reaction temperature is required to achieve high conversions under elevated pressures, as required by thermodynamics (Fig. S2, ESI). As carbon deposition rate increases with methane partial pressure [5], the increase in both reaction temperature and pressure would accelerate coke deposition kinetically. As a result, carbon gasification could become kinetically significant, therefore, severely endangering net carbon accumulation; (iii) at elevated temperatures and pressures, the cracking of methane in the gas phase could produce coke precursors, such as C_2H_2 , C_3C_4 olefins, C_6H_6 , etc., which are more susceptible to form coke on catalyst surfaces [6]. Thus far, it is only possible to operate DRM under either close to ambient pressure conditions (for instance, in commercialized Calcor process[7]) or under high pressure conditions in surplus of oxidant CO_2 (under sub-stoichiometric $\text{CH}_4:\text{CO}_2$ ratio of 1: 3, 14 bars, 800 °C, for up to 60 h [8].), and particular coke-resistant catalysts to process stoichiometric feed of CH_4 and CO_2 under high pressures still remain elusive.

Methane, the major component of natural gas (including shale gas,

* Corresponding authors.

E-mail addresses: yanzhu@ecust.edu.cn (Y.-A. Zhu), yangyong@shanghaitech.edu.cn (Y. Yang), kakezhu@ecust.edu.cn (K. Zhu).

¹ These authors contributed equally to this work.

methane hydrates, and coal gas etc.) and biogas, is industrially valorized via syngas mediated conversions, of which the reactions generating syngas are known as reforming reactions (Table S1, ESI). Despite that steam reforming of methane (SRM) and DRM share similarities in reaction mechanism and kinetic features, the state-of-the-art catalysts for SRM can not be extended to DRM process for the relatively low H/C ratio in the feed that favors coke deposition thermodynamically [1]. Coke deposition stems from three possible side reactions (Table S1, ESI): CH₄ dissociation, CO disproportionation (also known as Boudouard reaction) or CO hydrogenation, and thermodynamic diagnosis indicates that at elevated temperatures CH₄ dissociation constitutes the main source of coke (Fig. S3). Mechanistically, CH₄ dissociates successively into CH_x (x = 1–3) and surface C*, and C* undergoes further carbon-carbon coupling and consecutive nucleation at under-coordinated sites to afford encapsulating or whisker carbon (also referred to as filamentous carbon) [9,10], as illustrated in Scheme 1. Formation of whisker-like carbon should be avoided as whisker carbon has strong mechanic strength and is capable of pushing metal particles towards leaving their supports, which often causes catalyst pellet pulverization, clogging of tubular reactor and shut-down of operations [9]. In addition, hotspots can also occur as catalyst deactivates and no longer catalyzes the endothermic reaction. On perspective that carbon nucleation often entails the presence of under-coordinated surface sites and large ensemble size [9,11,12], numerous efforts have been devoted to combating coke deposition through: (i) introducing promoters that preferentially occupy under-coordinated sites (such as S in Sulphur passivated methane reforming process, known as SPARG process [13], Au [14], Sn [15], Ag [16], etc.), (ii) generating and maintaining tiny metallic nanoparticle size through ensemble size control, such that merely unstable, readily gasifiable soft carbon could form on catalyst surface, using preparations like exsolution methods from solid oxide solution precursors [17], (iii) accelerating surface coke oxidation by alloying with a second metal (such as Co [18], Fe [19], etc.). Most of these investigations are conducted at ambient pressures and only a few studies are devoted under pressurized conditions (as summarized in Table S2, ESI), and even less report characterizations of spent catalysts or residue coke, therefore, the robustness of these catalysts awaits further clarifications.

Compared with Ni or noble metal catalysts, fewer investigations have been carried out on Co-based catalysts [20,21], especially under more critical, pressurized conditions. According to theoretical envisages, coke deposition rate correlates with carbophilicity, i.e., the binding energy of carbon atoms on metal surfaces to form surface C*, while coke gasification rate is hinged to oxophilicity, viz, the binding energy of oxygen atoms on metal surfaces towards O* formation [22,23], obeying a 2-dimensional scaling relationship, and an ideal catalyst should possess well balanced carbophilicity and oxophilicity. Among transition metals, Ni and Co situate close to the optimal values from the volcano plots of turnover frequency (TOF) for DRM [24]. Co surface is predicted to be more oxophilic than Ni (by a factor of 0.14 eV) [22], which has a strong oxygen affinity over carbon, hence, either coke deposition (often on large Co particles with a large ensemble size of terrace sites [12]) or surface oxidation (on small Co particles with dominant

under-coordinated sites [25]) can be the cause of Co catalyst deactivation if its surface property is imbalanced. Alloying or other modification methods are promising to regulate Co properties to satisfy the requirements of DRM under pressurized conditions [3].

In this contribution, we demonstrate by combined time-on-stream (TOS) catalytic evaluation, characterizations of catalysts and deposited carbon, kinetic studies and theoretical rationale that Co-Rh intermetallic clusters are applicable as a coke-resistant DRM catalyst at 850 °C and 20 bars under diluent gas-free, equimolar stoichiometric feeding of CH₄ and CO₂ conditions. Our studies demonstrate that surface oxidative deactivation of Co can be retarded by an increase of operating pressure and co-presence of Rh. Enhanced coke-resistant property and TOS stability can be attained on catalyst with nominal Co/Rh ratio of 1. Surface-segregation-free Co₁Rh₃ intermetallic clusters are disclosed to be the active phase by semi *in situ* X-ray Photoelectron Spectroscopy (XPS) and comparisons with control samples. Microkinetic analysis derived from Density Functional Theory (DFT), together with experimental kinetic studies, show that the most abundant reaction intermediates (MARIs) are balanced C* and O* of low coverages. Moreover, on Co₁Rh₃ cluster surface, C* nucleation and transformation to recalcitrant graphene-like carbon is suppressed owing to a strain effect, allowing only the formation of CO₂ oxidative, soft carbon as intermediate.

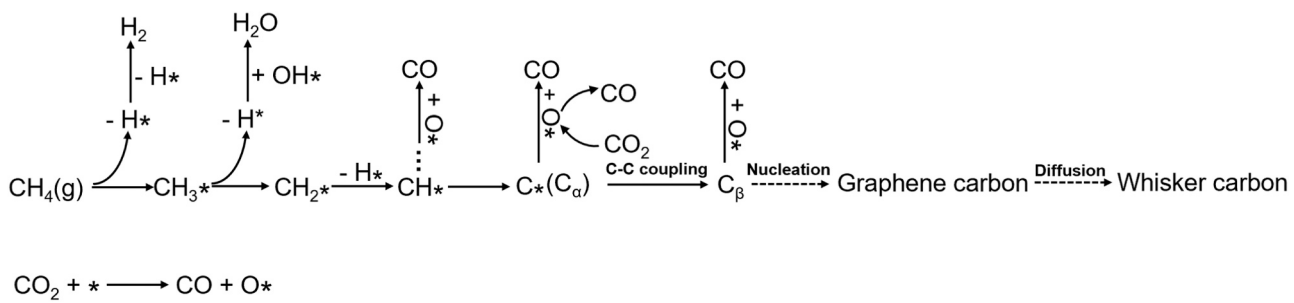
2. Experimental section

2.1. Materials

Magnesium acetate tetrahydrate (Mg(CH₃COO)₂·4H₂O, 99.0 %) was provided by Shanghai Titan Scientific Co. Ltd. Aluminum nitrate nonahydrate (Al(NO₃)₃·9H₂O, 99.0 %), citric acid (99.5 %), ethylene glycol (99 %), cobalt nitrate hexahydrate (Co(NO₃)₂·6H₂O, 99.99 %), ammonium hexachlororhodate ((NH₄)₂RhCl₆, 27.5 wt% of Rh) were purchased from Shanghai Macklin Biochemical Co. Ltd. Gases including methane (CH₄, 99.999 %), carbon dioxide (CO₂, 99.995 %), nitrogen (N₂, 99.999 %), passivation gas mixture of 99 % argon and 1 % oxygen, reducing gas mixture of 5 % hydrogen and 95 % argon, air (99.9995 %, 20 %–21 % O₂/N₂), hydrogen (H₂, 99.999 %), as well as carrier gas argon (Ar, 99.999 %) were provided by Shanghai Air Liquid Reagent Co. Ltd. Carbon monoxide (CO, 99.9 %) was purchased from Shanghai Chunyu Reagent Co. Ltd. All chemicals were used directly without further purifications.

2.2. Catalysts preparation

The spinel support MgAl₂O₄ was synthesized in accordance with the reported Pechini synthesis [26]. Magnesium acetate, aluminum nitrate and citric acid with a molar composition of 0.02: 0.04: 0.50 were dissolved in 500 mL of deionized water and homogenized by stirring for 3 h. The mixture was transferred to an oil bath of 70 °C. Ethylene glycol was added under constant agitation to the above mixture dropwise to achieve a 60 wt% relative to the amount of citric acid. Afterward, the



mixture was magnetically stirred at 70 °C for an additional 30 min, heated to 120 °C by a ramp of 2 °C min⁻¹ to evaporate water, till a gel was formed. The resultant gel was aged at room temperature for 48 h, before calcining in a muffle furnace by a rate of 3 °C min⁻¹ from room temperature to 550 °C and soaked at the same temperature for 2 h to remove organics. The heating temperature was raised to 850 °C by the same heating rate and held for 6 h to generate the calcined spinel support.

Supported catalysts were prepared by impregnation method. In the control, monometallic Co/MgAl₂O₄ sample, the content of Co was kept to be 7 mol. % (with respect to the percentage of Co/Co + Mg). To make fair comparisons, the molar loadings of other samples were maintained to equate this value, and Co/Rh molar ratios were manipulated to be 9/1, 7/3 and 1/1, respectively, labeled as Co₉Rh₁/MgAl₂O₄, Co₇Rh₃/MgAl₂O₄, and Co₁Rh₁/MgAl₂O₄. In a typical synthesis of Co₁Rh₁/MgAl₂O₄ catalyst, magnesium aluminum spinel was dispersed in a 0.1 mol L⁻¹ aqueous solution of 100 mL of ammonium hexachlororhodate and cobalt nitrate, and was thoroughly homogenized at room temperature for 5 h by stirring. The above mixture was dried by rotary evaporation till dryness. The obtained powder sample was dried at 90 °C for 12 h in a convection oven, calcined at 850 °C for 6 h with a rate of 3 °C min⁻¹ in a muffle furnace to produce the calcined sample.

The calcined sample was reduced in reducing gas (5 % H₂ in Ar) flow of 60 mL min⁻¹ for 2 h at 850 °C with a heating rate of 5 °C min⁻¹ under argon atmosphere in a tube furnace. Next, the sample was cooled to room temperature in hydrogen atmosphere. Each sample was passivated in a mixture gas of O₂ and Ar (1 % O₂, 30 mL min⁻¹) at room temperature before exposing it to air.

2.3. Catalyst characterizations

The phase composition of the catalysts was performed by X-ray diffraction (XRD, Rigaku D/Max-RC) using Cu K α radiation (operating at 40 kV and 40 mA, λ = 1.54178 Å). The measurements were carried out with a step time of 1.2 s and step increment of 0.02° in the 2 θ angle ranging from 10° to 80°. Transmission Electron Microscope (TEM) measurements were performed on a Spherical Aberration Electron Microscope Tecnai G2 F20 U-Twin microscope instrument operated at 200 kV, located in Suzhou Institute of Nano-Tech and Nano-bionics, Chinese Academy of Sciences. High-Angle Annular Dark Field-High Resolution Transmission Electron Microscope (HAADF-HRTEM) images were performed on the instrument operated at 200 kV. Energy dispersive X-ray spectroscopy (EDS) mapping was carried out using FEI Themis Z at 200 kV. The powder samples were prepared via dispersion in ethanol and spread over 100–200 mesh copper grids with support films on double folding grids. The metal particle size distributions were deduced by statistical analysis of assumed spherical metal particles from over 100 reduced metal particles in the TEM images using Nano Measurer 1.2, according to the formula (1):[22].

$$d_s = \frac{\sum n_i d_i^2}{\sum n_i d_i} \quad (1)$$

Where d_s is the average size of particles, n_i is the number of particles with diameter d_i .

Specific surface areas were deduced from N₂ physisorption isotherm measurements using the standard Brunauer-Emmett-Teller (BET) model. Before measurements, all samples were subject to degassing at 350 °C for (24 h) under vacuum (7.6 × 10⁻⁶ Torr) to remove surface contaminants. Inductively Coupled Plasma Atomic Emission Spectrometer (ICP, Agilent 725 ICP-AES) was used to determine the composition of the catalysts. H₂-temperature programmed reduction (H₂-TPR) curves were obtained in a Micromeritics Auto Chem II2920 instrument by heating the samples from 25 °C to a maximum of 1050 °C, under 30 mL min⁻¹ of H₂ (10.0 vol%)/Ar with a ramp of 10 °C min⁻¹. In each experiment, 100 mg of catalyst was used.

XPS analysis was performed by using a Thermo-Fischer ESCALAB 250Xi photoelectron spectrometer, applying mono-chromated Al K α ($h\nu$ = 1486.7 eV) X-ray irradiation and a 180 ° double focusing hemispherical analyzer with a six-channel detector. The base pressure of the instrument during the measurements was kept at 10⁻⁹–10⁻⁸ Torr. The raw data processing was performed by Thermo Avantage software. The binding energy scale of the recorded spectra was calibrated using the adventitious carbon C 1 s peak at 284.8 eV. The calcined samples were also treated under H₂ and reacting atmosphere in high pressure gas cell, UHV-connected with XPS analysis chamber. The in situ pre-cleaning procedure was described as follows. First, the calcined catalysts were heated to 800 °C in Ar flow (3 mL min⁻¹) and held for 30 min in H₂ (6 mL min⁻¹). Then, after cooling to room temperature in Ar atmosphere, the samples were transferred in-vacuum (10⁻⁷ mbar) into the XPS spectrometer. The spectra acquired for reduced samples were denoted with parenthesis to show the treatment atmosphere, for instance, Co/MgAl₂O₄(H₂). Further, the reduced samples were heated to 800 °C in Ar (3 mL min⁻¹) and feeding gases were introduced. The total feed gas flow rate to the reactor was set to be 20 mL min⁻¹ (GHSV = 120, 000 mL h⁻¹ g-cat⁻¹), with a stoichiometric feeding ratio of CH₄: CO₂ = 1: 1. After the heat was cut off, the samples were cooled in the reaction gas atmosphere. The corresponding spectra were labeled as Co/MgAl₂O₄(CH₄ + CO₂). To avoid surface contaminations upon exposing to the air, due to interaction with the atmosphere, each step was conducted inside air-proof based research facility platform on the ShanghaiTech University. Mg KLL Auger signal peak appears between 300 eV and 320 eV, overlapping with Rh 3d signal within 304–315 eV [27]. As Mg presented in the considered samples, to make a clearer conclusion on Rh behavior, we have made experiments using Mg K α X-ray source.

Chemisorption was employed to determine the number of exposed metal sites, based on which TOF numbers were generated. In each experiment, 100 mg of catalyst was used for H₂ titration. The sample was heated from room temperature to 850 °C by a ramp of 10 °C min⁻¹ under 10 vol% H₂/Ar with a flow rate of 30.0 mL min⁻¹ and kept for 2 h. After the reduction step, the catalyst was cooled to room temperature under ultra-high-purity Ar conditions. In the titration process, H₂ pulses were charged over the reduced catalyst and the H₂ uptake was monitored by a thermal conductivity detector (TCD). The stoichiometry number of H to surface Co or Rh was 1 [28,29]. To determine the type and amount of carbon deposition over spent catalysts, Thermal gravimetric analysis (TGA) were first performed using thermogravimetric analyzer Pyris 1 TGA (Perkin Elmer) in CO₂ from room temperature to 850 °C to determine the amount of gasifiable carbon. After CO₂-TGA was completed, the sample was heated to 850 °C under an air atmosphere. All the procedures were introduced in the flow of 50 mL min⁻¹ at a heating rate of 10 °C min⁻¹.

2.4. Catalytic assessments

The assessments of the catalytic performance were conducted at the pressures of 1–20 bars in a fixed-bed reactor made of corundum with an inner diameter of 8 mm, in a setup described previously [30]. The calcined catalyst of 40.0 mg was pressed, ground and sieved to obtain 40–60 mesh particles, which was diluted with 0.80 g silicon carbide of the same mesh for catalytic evaluations. The evenly dispersed mixture of catalyst and diluent was mounted by quartz wool in the quasi-isothermal zone of the reaction tube. The upstream of the catalyst was arranged with two sizes of alumina pellets with diameters of 3 mm (12.00 g) and 5 mm (6.00 g) to promote heat exchange of the reaction gas before reaching the catalyst bed. A corundum tube with an outer diameter of 6 mm was attached to the downstream of the catalyst to support the whole catalyst bed. N₂ (10.00 mL min⁻¹) was used to fill the space between the concentric corundum tube and the stainless steel tube, which was set to a pressure equivalent to that of the reaction gas, in order to balance the internal and external pressure across the corundum tube and prevent the effect of metal dust when the metallic reactor was in direct

contact with reaction mixtures. The reactor temperature was raised from room temperature to 850 °C at a heating rate of 5 °C min⁻¹ and in a flow of N₂ (30.00 mL min⁻¹). Upon reaching the presetting temperature, the gas was switched to H₂ (60.00 mL min⁻¹) and kept at 850 °C for 2 h to reduce the catalyst to the metallic state. After reduction pretreatment, the feeding gases were introduced. The total feed gas flow rate to the reactor was set to be 60.00 mL min⁻¹ (GHSV = 90, 900 mL h⁻¹ g-cat⁻¹), with a stoichiometric feeding ratio of CH₄: CO₂ = 1: 1 under diluent-gas free reaction conditions. A co-feeding of 1.00 vol% H₂ was applied to prevent possible oxidation of catalyst surface, which was a common practice in industrial operations. The total pressure of the system was increased stepwise from ambient to 20 bars, with an increment of 5 bar per step, and was maintained at each stage for 12 h TOS test. The effluent gas composition was analyzed by an on-line GC-9560 (Shanghai Ai Hua Instrument), equipped with a TDX-01 column and a TCD. CH₄, CO₂ conversions and the H₂/CO ratio are defined as follows:

$$X_{CH_4} (\%) = \frac{[CH_4]_{in} - [CH_4]_{out}}{[CH_4]_{in}} \times 100 \% \quad (2)$$

$$X_{CO_2} (\%) = \frac{[CO_2]_{in} - [CO_2]_{out}}{[CO_2]_{in}} \times 100 \% \quad (3)$$

$$H_2 / CO = \frac{[H_2]_{out}}{[CO]_{out}} \quad (4)$$

2.5. Kinetic studies

The evenly dispersed mixture of catalyst and diluent was mounted by quartz wool in the quasi-isothermal zone of the reaction tube. The influences of both internal diffusion and external diffusion on kinetic studies were strictly ruled out, as detailed in our previous work [31]. Catalyst and diluent spinel MgAl₂O₄ were mixed with a ratio of 1/10, which was pressed, ground and sieved to obtain 80–100 mesh particles. The mounted amounts of Co, Rh and bimetallic catalysts and diluent mixture were 20 mg, 50 mg and 990 mg, respectively, and the methane conversion was kept below 10 %. The upstream and downstream of the catalyst were arranged with silica of the same mesh. The catalyst and silica were mounted by quartz wool in the quasi-isothermal zone of the reaction tube. To investigate the reaction orders with respect to CH₄, CO₂, H₂, and CO, reaction rate variations with their partial pressures were carried out at 720 °C. Partial pressures of reactants CH₄ or CO₂ were manipulated between 20 kPa and 40 kPa and products H₂ or CO were regulated from 3 to 23 kPa, 10 to 30 kPa, respectively. The total pressure was kept constant (101 kPa) by adjusting the partial pressure of make-up gas N₂. Activation energies of monometallic Co, Rh and bimetallic Co₁Rh₁/MgAl₂O₄ catalysts were measured at steady state using Arrhenius plots collected at temperatures from 720 °C to 800 °C, 640 °C to 720 °C and 680 °C to 760 °C, respectively, with feeding gas (molar ratio of CH₄: CO₂: N₂: H₂ = 20: 20: 58: 3) flow rate of 101.00 mL min⁻¹.

2.6. Computational details

The DFT calculations were performed with Vienna Ab initio Simulation Package [32]. The exchange and correlation of the Kohn-Sham theory was treated with the BEEF-vdW [33] functional. The projector-augmented wave method [34] was used to describe the interactions of valence electrons with ion cores. The first Brillouin zone of the slab model was sampled using a Monkhorst-Pack grid [35]. The energy cutoff was set to 400 eV in the calculations. The Methfessel-Paxton scheme is used with an energy smearing of 0.2 eV to determine the partial electron occupancies [36]. Adsorbates are relaxed until the forces are less than 0.03 eV/Å. Transition-state geometries were searched by the dimer method [37], and the transition states were verified by frequency calculations in which only one imaginary

frequency was obtained for each transition state.

Slab models were first built on the face-centered cubic (fcc) transition metals including Co and Rh, with the (111) and (211) surfaces modeling the terraces and steps of fcc nanoparticles. The (111) surfaces were modeled as a 5-layer slab having a *p* (3 × 3) supercell. As for the (211) surfaces, we used a 15-layer slab having a *p* (1 × 3) supercell. The bottom two and six layers in the slabs of (111) and (211) surfaces were fixed. The bottom two layers in the slabs were fixed at the bulk structure and all the other atoms in the slabs were allowed to relax. A vacuum space of 12 Å was used to avoid periodic interactions between two neighboring slabs. The first Brillouin zone of the slabs was sampled with a 5 × 5 × 1 and a 5 × 3 × 1 Monkhorst-Pack grid.

For Co₁Rh₃ alloy, a rectangular (2√3 × 2) supercell with eight metal atoms per layer was used to represent the Co₁Rh₃(111) surface. The surface was modeled as a 5-layer slab and the bottom two layers in the slabs were fixed. The Co₁Rh₃(211) surface were represented as a 16-layer slab, which has a *p* (1 × 2) supercell and consists of 32 atoms. There were two atomic arrangements on Co₁Rh₃(211) surface, which named Co₁Rh₃(211)_a and Co₁Rh₃(211)_b. The bottom seven layers in the slabs were fixed. The first Brillouin zone of these alloy slabs were sampled using a 5 × 7 × 1 Monkhorst-Pack grid.

Table S9 shows the reaction network of the DRM identified in this work. CH₄ activation and successive dehydrogenation to produce CH₃^{*}, CH₂^{*}, CH^{*} and C^{*} are represented as steps 1–4, co-producing H^{*}. CH^{*} coupling with O^{*} (step 12) to yield HCO^{*} followed by HCO^{*} dehydrogenation to produce CO^{*} (step 13), C^{*} coupling with OH^{*} to COH^{*} (step 10) and its decomposition to CO^{*} (step 11) and C^{*} coupling to O^{*} to CO^{*} (step 14) are considered as the main gasification routes from CH₄ to CO-H₂O are generated by recombination of H^{*} and OH^{*} (steps 15, 16). Two surface H^{*} are coupled into gas H₂ (step 18). Besides, there are different CO₂ activation pathways in the reaction network. CO₂ activation through direct dissociation (step 5) to CO^{*} and O^{*} or H^{*} -assisted activation to produce COOH^{*} (step 6) and HCOO^{*} (step 7). COOH^{*} is further decomposed into CO^{*} and OH^{*} (through step 9). HCOO^{*} (via steps 8) eventually is decomposed into O^{*} and HCO^{*}. Other steps involving formation and consumption of intermediates, as well as adsorption or desorption steps, are also outlined.

The microkinetic analysis in this work was carried out using a modified CatMAP code [38]. We calculated the TOFs of all elementary steps by solving a mean-field model with coupled differential equations under steady-state approximation. For the gas-phase species, the Shomate equation was used to calculate the enthalpy (H⁰) and entropy (S⁰), with the Shomate parameters obtained from the NIST database [39]. For reaction intermediates and transition states, the enthalpy and entropy were estimated under harmonic approximations as implemented in the ASE package [40]. The rate constant (*k*) of elementary steps were obtained by using the same method proposed in our previous work [41].

The rate constant (*k*) for elementary steps was evaluation based on the transition state theory, which can be expressed as

$$k = (k_B T / h) \exp(S^\ddagger / k_B T) \exp(-H^\ddagger / k_B T) \quad (5)$$

where *k_B* is the Boltzmann's constant, *h* is the Planck's constant, *S*^{ddagger} is the standard entropy change from the initial to the transition state, *H*^{ddagger} is the standard enthalpy change from the initial to the transition state, and *T* the reaction temperature.

The TOFs of elementary steps were determined by invoking the steady-state approximation and by numerically solving the coupled differential equations. The differential equations are written as

$$r_i = k_i^+ \prod_n \theta_{in} \prod_n p_{in} - k_i^- \prod_l \theta_{il} \prod_l p_{il} \quad (6)$$

$$\partial \theta_j / \partial t = \sum_i s_{ji} r_i \quad (7)$$

where r_i is the rate for each elementary step, the forward rate constant, the reverse rate constant θ_{in} and θ_{il} are the surface concentrations of the reactant and product for elementary step i , p_{in} and p_{il} are the unitless pressure of the gas-phase reactant and product for elementary step i , and s_{ji} is the stoichiometric coefficient of species j in elementary step i . This set of coupled non-linear ordinary differential equations has a steady-state solution as

$$\frac{\partial \theta_j}{\partial t} = 0 \quad (8)$$

which can be solved subject to the site conservation constraint:

$$\sum_j \theta_j = \theta^{TOT} \quad (9)$$

where θ^{TOT} is the normalized surface area.

The simulation temperature was set to 850 °C and the total pressure was 20 bars. The ratio between CH₄ and CO₂ in the gaseous reactant was 1:1. The reaction order (n_x) on Co(111), Rh(111) and Co₁Rh₃(111) can be calculated as follow.

$$n_x = \frac{\partial \ln r}{\partial \ln [X]} = [X] \frac{\partial \ln r}{\partial [X]} \quad (10)$$

Where r is the reaction rate and X is pressure of the gas involved in DRM.

We made an infinite graphene overlayer on surface(111) as model shown in Fig. S27b to calculate the energy of a carbon atom on the graphene-covered surface, the equation are expressed as

$$E_{\text{graphene}} = \frac{E_{\text{surface+graphene overlayer}} - E_{\text{surface}}}{N_{\text{graphene}}} \quad (11)$$

Here, E_{graphene} is the energy of a carbon atom on the graphene-covered surface, $E_{\text{surface+graphene overlayer}}$ is the total energy of surface and graphene overlayer, E_{surface} is the total energy of the clean surface slab, N_{graphene} denotes the number of carbon atoms in the unit cell. Moreover, we performed DFT calculations on the structure shown in Fig. S27a to estimate for the edge energy of the graphene edge of the island. The energy of an edge carbon relative to E_{graphene} was calculated as

$$\Delta E_{\text{edge}} = \frac{E_{\text{surface+graphene edge}} - E_{\text{surface}} - N_{\text{graphene edge}} \times E_{\text{graphene}}}{N_{\text{edge}}} \quad (12)$$

where ΔE_{edge} is the energy of an edge carbon relative to E_{graphene} , $E_{\text{surface+graphene edge}}$ represents the total energy of surface and graphene with edge carbon atoms, $N_{\text{graphene edge}}$ denotes the number of carbon atoms in the unit cell, N_{edge} is the number of edge carbon atoms of graphene. The energy of an adsorbed carbon on surface was calculated as

$$E_{\text{atomicC}} = E_{\text{atomicC+surface}} - E_{\text{surface}} \quad (13)$$

where $E_{\text{atomicC+surface}}$ is the total energy of surface and one adsorbed carbon atom. The relative energies of one carbon atom on surface(111), surface(211) and the graphene-covered surface and ΔE_{edge} on surface (111) are given in Table S10. Here, we set the zero of energy to carbon adsorbed at the surface (211).

3. Results and discussion

3.1. Formation and characterizations of Co-Rh alloy particles as active phase

Co-Rh/MgAl₂O₄ series samples were prepared with manipulated Co/Rh ratios to be 9/1, 7/3 and 1/1, respectively. MgAl₂O₄ was selected as catalyst support to avoid possible reactions between the contacting gas and the support (Table S3, ESI). The loading of Co in the control Co/MgAl₂O₄ sample was kept to be 7 mol. % (i.e., Co/Co + Mg) and the Co-Rh total molar contents in bimetallic samples were kept constant. Such low loadings guarantee that the metal clusters are small enough to

ensure better carbon tolerance, which is often size-dependent [11]. The structures of the calcined samples were monitored by XRD (Fig. S4) and XPS (Fig. S5), showing only crystalline support and surface oxides, for the high dispersions of supported metals.

As the loading 7 mol. % of Co and Rh in these samples were too low to form XRD detectable phases, a series of control samples with high metal loading of 20 mol. % and 40 mol. % and identical Co/Rh ratios were prepared for comparison, as illustrated in Fig. S6. H₂-TPR measurements were compared with the high loading samples, to determine reducibility of calcined samples (Fig. S7). Together, they showed that Co-Rh mixed oxides formed after calcinations and the two metals were simultaneously reduced into their metallic states, i.e., the two metals alloyed. Reduced 7 mol. % samples comprised of XRD undetectable metal clusters (Fig. S8), while the corresponding high loading samples (Fig. S9, 10) showed well resolved Co-Rh alloy diffractions that fit approximately Vegard's law of solid solution (Fig. S11), recommending formation of intermetallic clusters in bimetallic 7 mol. % samples. BET surfaces area shows that the surface area variations are small (between 59 and 78 m² g⁻¹) among samples, as reported in Table S4.

The TEM micrographs of reduced representative Co₁Rh₁/MgAl₂O₄ are outlined in Fig. 1. From the dark and bright field images (Figs. 1a, 1b), tiny metallic particles on the spinel support can be clearly visualized. White spots of 1.5–7.7 nm in diameter in the dark field image are the alloy particles. Metallic particle-size-distribution, as displayed in Fig. 1e, discloses size focused distribution with a weight average size of ca. 3.5 nm. From a selected metallic particle (Fig. 1c), lattice fringe of 2.1 Å, corresponding to (111) facet of Co₁Rh₃ alloy [42], could be identified. Line-scan and mapping of element distributions, as unveiled in Fig. 1(f, g, h), corroborate that the two metals are together. The TEM micrographs of monometallic Co/MgAl₂O₄ and Rh/MgAl₂O₄ samples are presented in Fig. S12, averaged 13.2 nm Co⁰ clusters (ranging from 7.7 to 23.6 nm) and 2.9 nm Rh⁰ (from 1.4 to 4.7 nm) particles could be deduced. It is seen that alloying leads to the formation of smaller Co-Rh clusters (whose size is close to Rh⁰ clusters) with respect to pristine Co⁰ clusters, owing to a reduced reduction temperature caused by H₂-spillover effect from Rh (Fig. S7). The same conclusion may be drawn from dispersion of metals acquired by H₂ titration (Table S4).

XPS measurements were undertaken to gain insight regarding the oxidation states and surface elemental compositions of the catalysts. The data for representative Co/MgAl₂O₄, Co₁Rh₁/MgAl₂O₄ and Rh/MgAl₂O₄ samples were recorded after in situ pretreatment in H₂ (800 °C, 30 min). The XPS spectra for H₂-reduced samples were also compared with those obtained after in situ interaction with the reaction atmosphere (CH₄: CO₂ of 1: 1, total pressure of 6 bar, total flow rate of 20 mL min⁻¹ for 10 min, at 800 °C), as demonstrated in Fig. 2. The XPS analysis was performed without exposing to air, to avoid possible surface oxidation or structure changes. The Rh 3d spectrum of the reduced Rh/MgAl₂O₄ sample shows mainly metallic Rh⁰ (Rh 3d_{5/2} 307.2 eV, 80 at%) in addition to a small amount of Rh³⁺ (310.5 eV, 20 at%) that strongly interacts with the support being resistant to the reduction. The Co 2p spectrum of the reduced Co/MgAl₂O₄ demonstrates the presence of Co⁰ (Co 2p_{3/2} 777.9 eV, 30 at%) [43] and Co²⁺ (781.6 eV, 70 at%) [44] expected in the form of dissolved CoAl₂O₄. More Co⁰ (38 at%, 778.9 eV) is determined on the reduced bimetallic Co₁Rh₁/MgAl₂O₄ sample, compared to the monometallic Co/MgAl₂O₄, which is explained by the assisted reduction of Co²⁺ in the presence of Rh in a consequence of hydrogen spillover [45]. In the bimetallic sample, a major metallic Rh⁰ (307.2 eV, 70 at%) and a minor Rh³⁺ (310.7 eV, 30 at%) can be distinguished from Rh 3d spectra, showing that most of Rh has been reduced as the result of pretreatment. The small shift of Co⁰ and Rh⁰ peaks in spectra of Co₁Rh₁/MgAl₂O₄ with respect to that of monometallic ones implies a charge transfer from Co to Rh in the result of alloying, due to their differed electronegativity. Upon contacting with reaction atmosphere, the portion of metallic Co⁰ in Co/MgAl₂O₄ (22 at%) and Co₁Rh₁/MgAl₂O₄ (31 at%) samples decreases slightly if compared to that recorded after H₂ reduction. The same tendency can be

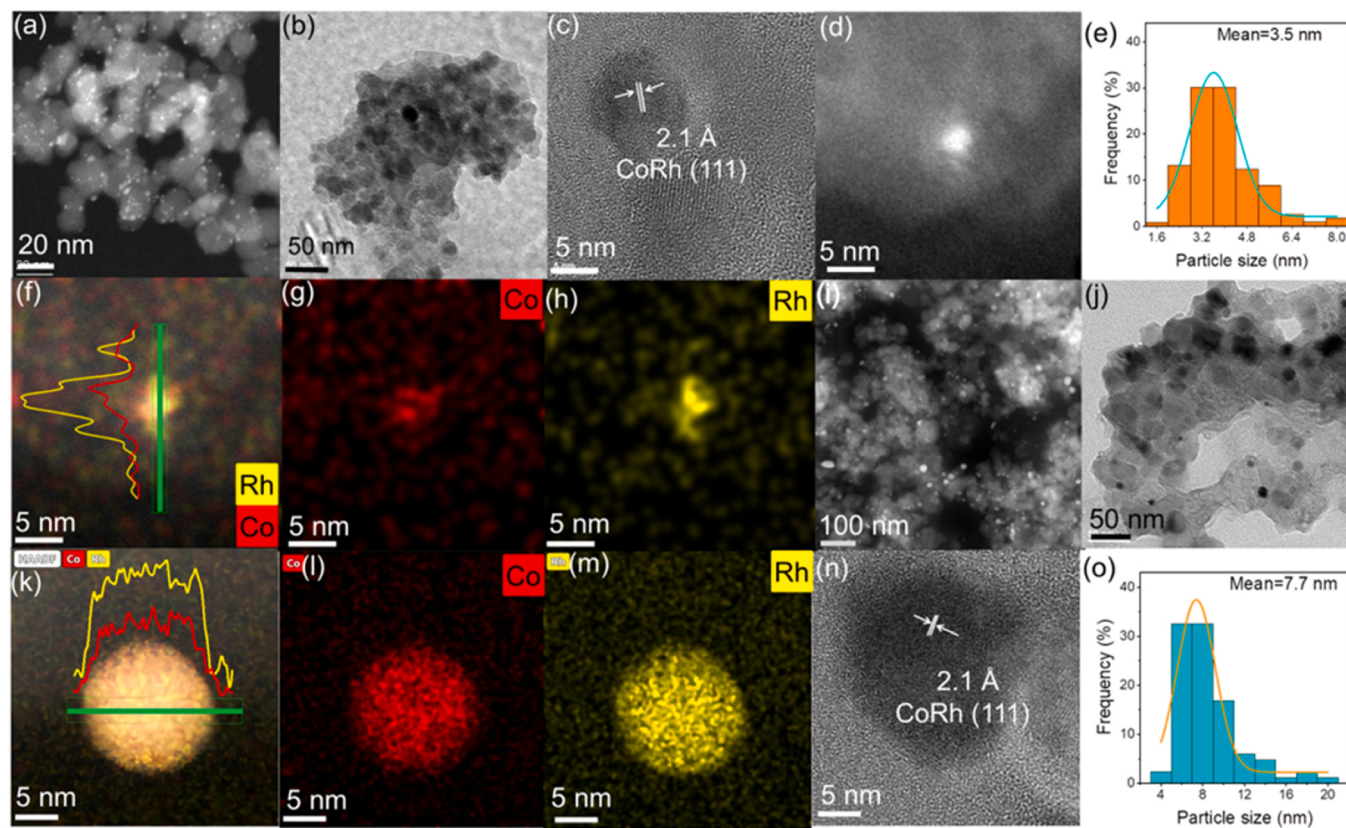


Fig. 1. Dark, bright field TEM micrographs, particle-size-distributions and element mapping for fresh (a-h) and spent (i-o) $\text{Co}_1\text{Rh}_1/\text{MgAl}_2\text{O}_4$ catalyst.

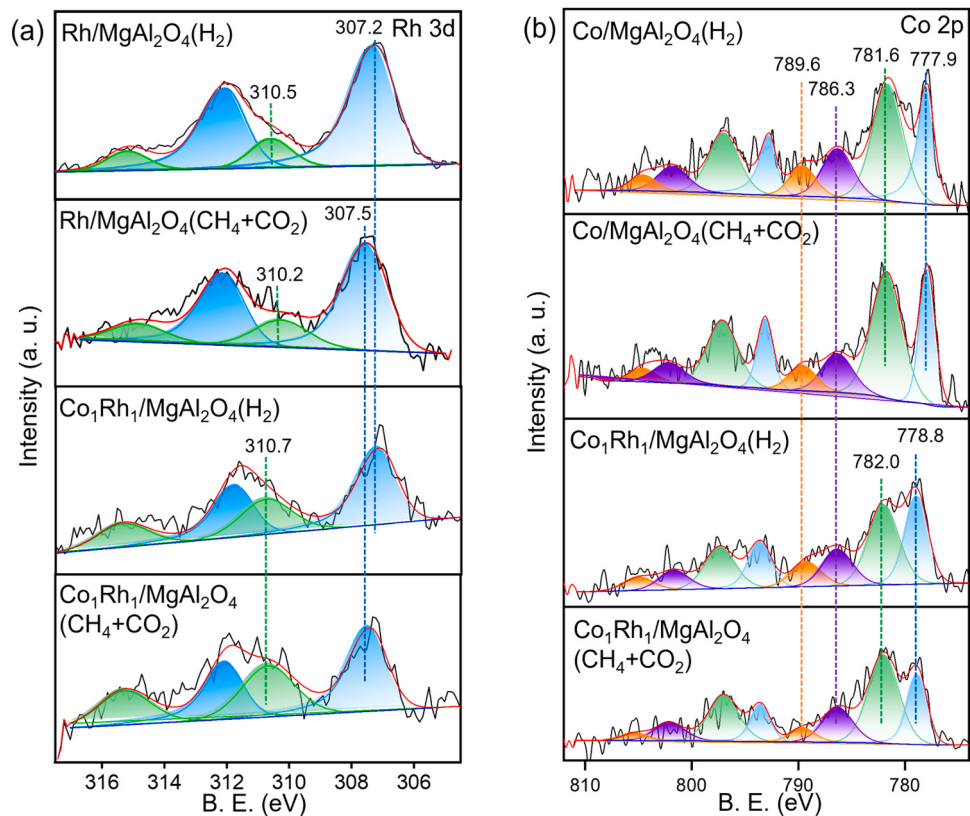


Fig. 2. Rh 3d Rh 3d (a) and Co (2p) XPS spectra. The calcined catalysts were reduced in H_2 (6 mL min^{-1}) for 30 min and the treatment atmosphere is marked in parenthesis. Further, the reduced samples were contacted with feeding reactants ($\text{GHSV} = 120,000 \text{ mL h}^{-1} \text{ g-cat}^{-1}$), in a stoichiometric ratio of $\text{CH}_4: \text{CO}_2 = 1:1$.

inferred for $\text{Rh}^0/\text{Rh}^{3+}$ ratio (changing from 2.3 to 1.3 and from 4.0 to 2.5 for $\text{Co}_1\text{Rh}_1/\text{MgAl}_2\text{O}_4$ and $\text{Rh}/\text{MgAl}_2\text{O}_4$ samples, respectively, Table S6), comparing spectra of H_2 reduced samples and spectra of the samples after exposing to the reaction atmosphere.

The quantitative analysis of surface compositions is shown in Table S6, S7 and Fig. S13. The metallic Rh^0/Co^0 ratio after treatments in H_2 and reaction atmosphere is disclosed to be 2.7 and 3.3, respectively, which is close to the value of 3, corresponding to the nominal composition of Co_1Rh_3 alloy. As XPS is a surface sensitive technique, the results demonstrate that there is essentially no surface segregation under both H_2 and reacting atmospheres. Since surface segregation is favored at low temperatures [46], it is logical to expect that segregation should be negligibly small at the reaction condition and high temperatures.

3.2. Catalytic stability and coke-resistant properties under elevated pressures

Through blank tests (Fig. S15), it was seen that contribution of methane gas phase cracking is negligibly small in the absence of catalyst at low pressure of 1 bar, but could contribute more at elevated pressures. The co-feeding of H_2 was found to have minimized the impact of methane cracking, in particular at elevated pressures. The impact of co-fed 1 vol% H_2 in the feeding gas on the overall catalytic performance was evaluated using $\text{Co}/\text{MgAl}_2\text{O}_4$ catalyst (Fig. S14), and marginal effect on product composition was measured.

The catalytic stabilities are displayed, as plots of CH_4 , CO_2 conversions and H_2/CO ratios against TOS in Fig. 3a, b and c. Monometallic $\text{Co}/\text{MgAl}_2\text{O}_4$ catalyst exhibits rather low (< 3.59 %) CH_4 conversion at 1 bar, possibly because of re-oxidation of Co surface on contacting with CO_2 [47]. The activity of this catalyst increased significantly to ca. 72.20

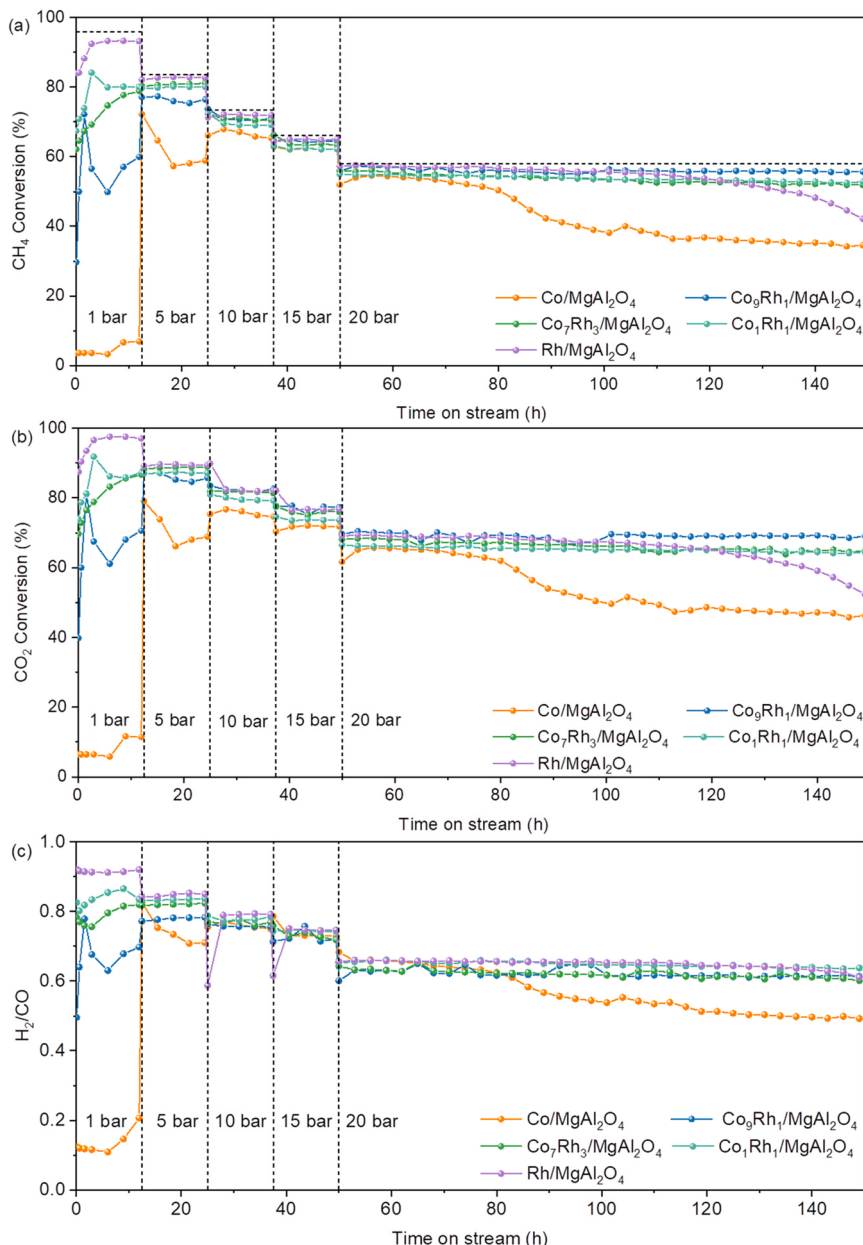


Fig. 3. TOS stability as functions of (a) CH_4 conversion, (b) CO_2 conversion and (c) the corresponding H_2/CO ratio in product. The TOS stabilities of monometallic catalysts are also shown for comparison. Pressure is increased in a stepwise manner with a step of 5 bar. Reaction conditions: catalyst loading of 40 mg, 850 °C, 1.0–20 bars, space velocity of 90, 900 $\text{mL h}^{-1} \text{g-cat}^{-1}$. The dashed line in (a) indicates the equilibrium conversion of CH_4 .

% when the pressure is increased to 5 bars and relatively stable conversions can be noticed at elevated pressures between 10 and 15 bars. However, the TOS stability only lasts for 30 h at 20 bars, and the initial conversion dropped from ca. 54.36–35.61 % after 70 h. Surface oxidative deactivation of Co^0 is herein found to be overcome by pressure increase. This pressure dependent catalytic activity variation has not been reported previously. The implication is that low catalytic activity for Co^0 clusters at ambient pressure does not hamper its use under high pressure operations. The pressure compensation shall be considered for high pressure catalyst design.

The catalytic activities for $\text{Co}_9\text{Rh}_1/\text{MgAl}_2\text{O}_4$, $\text{Co}_7\text{Rh}_3/\text{MgAl}_2\text{O}_4$, $\text{Co}_1\text{Rh}_1/\text{MgAl}_2\text{O}_4$ and $\text{Rh}/\text{MgAl}_2\text{O}_4$, increase proportionately with increasing Rh content at all pressures, as surface oxidative deactivation has been alleviated by H_2 spillover in the presence of Rh. Under pressurized conditions of 20 bars, activity for $\text{Rh}/\text{MgAl}_2\text{O}_4$ declines from 70 h on, and a conversion loss of 15.03 % (from initial activity of 57.19% to 42.16 % at the end) can be estimated. In contrast, all bimetallic catalysts show TOS stability during the 100 h period test, and activity loss in CH_4 conversions can be inferred to be low for $\text{Co}_9\text{Rh}_1/\text{MgAl}_2\text{O}_4$ (from 55.76 % to 55.65 %), $\text{Co}_7\text{Rh}_3/\text{MgAl}_2\text{O}_4$ (from 55.93 % to 51.89 %) and $\text{Co}_1\text{Rh}_1/\text{MgAl}_2\text{O}_4$ (from 54.97 % to 52.82 %). On all catalysts, a higher CO_2 conversion is determined, as a consequence of reverse-water-gas-shift (RWGS), which is rapid and is considered to be equilibrated [5]. For the same reason, H_2/CO ratio in the syngas product is dependent on thermodynamics, i.e., CH_4 conversion and operation conditions, rather than kinetics (catalyst used). $\text{Co}_1\text{Rh}_1/\text{MgAl}_2\text{O}_4$ maps out as the outstanding stable catalyst among others and the stability is reproducible (Fig. S1). It is noteworthy at this point that the apparently stable TOS conversion alone does not adequately show that a catalyst is coke-resistant, as whisker carbon growth does not necessarily lead to activity loss [9,48]. Therefore, an autopsy analysis of spent catalysts, specifically, the nature and amount of deposited carbon, is necessary to prove coke tolerance of catalysts.

3.3. Characterizations of spent catalysts

In XRD patterns of spent samples (Fig. S17), one weak peak at $2\theta = 26.60^\circ$ belonging to diffraction from (003) plane of graphite carbon (JCPDS No. 26–1079) [9,48] can be identified in all the catalysts, except for $\text{Co}_1\text{Rh}_1/\text{MgAl}_2\text{O}_4$. As graphite is associated with encapsulating or whisker carbon that is generated by surface carbon nucleation and growth [11], the absence of graphite carbon implies that the catalyst possesses outstanding coke-resistant property.

From TEM micrographs for spent $\text{Co}_1\text{Rh}_1/\text{MgAl}_2\text{O}_4$ (Figs. 1i, 1j), no encapsulating or whisker carbon has been detected. Clusters ranging from 2.6 to 18.4 nm, with a mean size of ca. 7.7 nm, can be estimated based on the dark field measurement of metallic clusters, as reported in the histogram in Fig. 1o. To reveal the alloy nature of these clusters, a line-scan of elemental composition is conducted on a typical metallic particle, as displayed in Fig. 1k, evidencing that the two metals are homogeneously distributed and the Rh content is far rich than Co, and superimposable mapping patterns are detected (Fig. 1k, l, m). A lattice fringe of ca. 2.1 Å, assignable to (111) planes of Co_1Rh_3 alloy, is determined on the cluster. In contrast, whisker carbon is detectable in the spent $\text{Rh}/\text{MgAl}_2\text{O}_4$ catalyst (Fig. S18), as marked by a red arrow, while no whisker is visualized on $\text{Co}/\text{MgAl}_2\text{O}_4$. A prominent increase of Co^0 particle size from ca. 13.2 nm (Fig. S12c) of fresh catalyst to 24.4 nm (Fig. S18d) is calculated, suggesting sintering is likely the cause of activity loss. By comparison, it is seen that alloying has alleviated sintering of metallic clusters and insignificant deactivation has been observed in the TOS test. XPS measurements unravel the surface Co^0/Rh^0 ratio over spent $\text{Co}_1\text{Rh}_1/\text{MgAl}_2\text{O}_4$ catalyst is close to 1/3 (Fig. S19, Table S8) and the sample has the least graphite carbon with respect to monometallic catalysts.

TGA under successive CO_2 and air atmosphere were collected for spent catalysts. It is assumed that the deposited soft carbon can be

reacted off under CO_2 atmosphere, whilst the rest refractory one can only be scavenged by O_2 [49]. Fig. S20a describes weight loss curves in CO_2 -TGA process, showing that the onset temperature for soft carbon oxidation starts from 230 °C and ends at 820 °C. The TGA-air curves are depicted in Fig. S20b, and only traces of refractory carbons were determined. Quantitative analyses of decomposed types for deposited carbon are extracted and displayed in Fig. S20e. The data disclose that the amount of total carbon deposits on monometallic $\text{Co}/\text{MgAl}_2\text{O}_4$ is the lowest (5.01 wt%), but it contains the largest fraction of refractory type (0.35 wt%). All other spent catalysts are essentially refractory carbon free. Over spent $\text{Rh}/\text{MgAl}_2\text{O}_4$, the largest amount of deposited carbon (18.44 wt%) was measured, which presumably is responsible for the deactivation. $\text{Co}_1\text{Rh}_1/\text{MgAl}_2\text{O}_4$ has the lowest total carbon (9.60 wt%) deposits among bimetallic Co-Rh catalysts, and of solely soft type, which agrees well with TEM and XRD results.

3.4. Kinetic effect of alloying

In regard that carbon deposition on catalyst surface is a dynamic process, there should be no net carbon accumulation once carbon formation rate balances its removal rate. In order to parameterize the kinetic features of Co_1Rh_3 cluster catalyst, kinetic studies were undertaken under the differential reactor model. The dependences of reaction rate on partial pressures of reactants and products are determined over the representative $\text{Co}_1\text{Rh}_1/\text{MgAl}_2\text{O}_4$ catalyst, and compared with these of monometallic ones, as displayed in Fig. 4a-d. The measured CH_4 elimination rate at 720 °C increases proportionally to CH_4 partial pressure, obeying a first order reaction law. The reaction rate is found to be invariant to CO_2 partial pressure (Fig. 4b), viz, a zeroth-order dependence. The reaction rates, as a function of partial pressures of products, as depicted in Fig. 4c-d, for H_2 and CO , respectively, was found to be unchanged. It follows that the reaction law could be expressed as Eq. (14) on $\text{Co}_1\text{Rh}_1/\text{MgAl}_2\text{O}_4$ catalyst. The ordinates for the reaction rate was set to be the elimination rate of CH_4 , as CO_2 could also be consumed by RWGS reaction, while CH_4 is only converted through DRM under steady state operations [5]. The same reaction law is obeyed by $\text{Rh}/\text{MgAl}_2\text{O}_4$ catalyst.

$$r_M = k_M p_{CH_4} \quad (14)$$

Where r_M , k_M , and p_{CH_4} are, respectively, the reaction rate, the reaction rate constant for $\text{Rh}/\text{MgAl}_2\text{O}_4$ or $\text{Co}_1\text{Rh}_1/\text{MgAl}_2\text{O}_4$ (M=Co-Rh or Rh) and methane partial pressure. M indicates metal monometallic, rhodium or bimetallic Co-Rh.

Over $\text{Co}/\text{MgAl}_2\text{O}_4$ catalyst, a small negative order with respect to p_{CO_2} has been observed. Regarding the oxophilicity of Co surface, the rate law can be depicted as follows (the detailed derivations can be found from ESI):

$$\begin{aligned} r_{Co} &= k_{Co} p_{CH_4} (1 - \theta_{O*})^2 = k_{Co} p_{CH_4} \left(\frac{1}{1 + \frac{K_{CO_2} p_{CO_2}}{K_{Co} p_{CO}}} \right)^2 \\ &= k_{Co} p_{CH_4} \left(\frac{1}{1 + K' p_{CO_2}} \right)^2 \end{aligned} \quad (15)$$

Whereby K' is the corresponding dissociative adsorption constant for CO_2 , K_{CO} is the reaction rate constant for $\text{Co}/\text{MgAl}_2\text{O}_4$ catalyst, θ_{O*} is the oxygen coverage, K_{CO_2} and K_{CO} are the thermodynamic equilibrium constant for CO_2 adsorption and CO adsorption, respectively, p_{CO_2} , p_{CO} , are the partial pressures of CO_2 , and CO , respectively. As adsorption term in the denominator is found to be rather low ($K'_{CO_2} = 0.032 \text{ kPa}^{-1}$), the kinetic law could still be approximated by using Eq. 14. As the influence of CO_2 partial pressure is unimportant, reaction rate is mainly influenced by methane partial pressure variations. This kinetic law also explains that the pressure-dependent activity in the TOS test for the

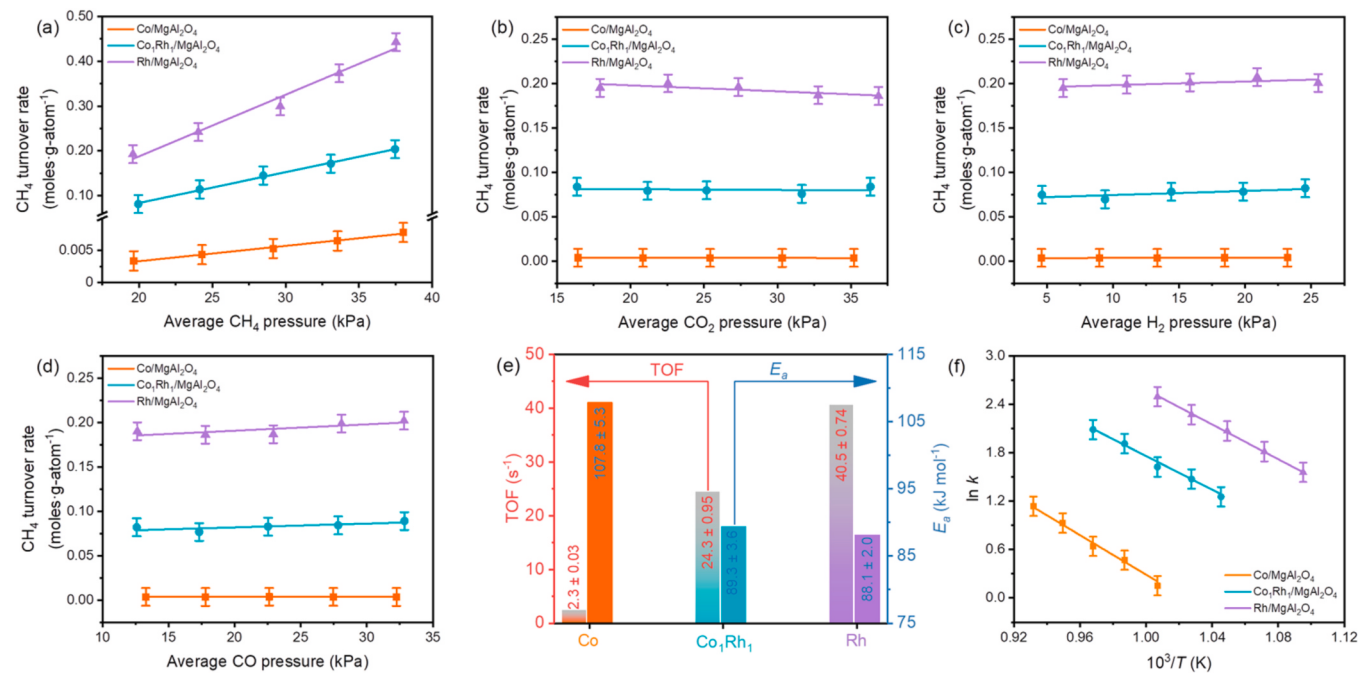


Fig. 4. Effects of CH₄ (a), CO₂ (b), CO (c), and H₂ (d) partial pressures on reaction rates over Co/MgAl₂O₄, Co₁Rh₁/MgAl₂O₄ and Rh/MgAl₂O₄. TOF values derived from the reaction rates at 720 °C, 1 atm and activation energies are shown in (e). Arrhenius plots are depicted in (f). The data were measured at each point three times and the error bars were generated thereof.

same catalyst, and compensation effect originates from increase of methane partial pressure and more H₂ has been produced that maintains the Co⁰ surface reduced.

The kinetic law for these catalysts proves that CH₄ dissociation is the elementary rate determining step in both DRM reaction and coke-deposition step and is in line with previous reports of kinetic features of Rh [50]. The absence of denominator terms related to metal surface adsorption contributions indicates that the surface is close to completely clean, i.e. a negligibly low surface coverage by reaction intermediates, except that a small concentration from O^{*} is detectable over Co surface. The steps related to the formation of CO and H₂ are linked by rapid RWGS reaction (reaction 7 in Table S1), which could be regarded as equilibrated under reforming conditions [5,18].

Turnover frequency values are extracted over all catalysts under the following conditions: 720 °C, 1 bar, CH₄/CO₂/N₂/H₂ = 20: 20: 60: 1, with a total gas flow rate of 101 mL min⁻¹ (GHSV = 151, 500 mL h⁻¹ g-cat⁻¹), while keeping the CH₄ conversion to below 10 %. The TOFs are normalized to surface atom numbers of either Co or Rh, obtained from chemical titration by H₂ (Table S4). Since the two metals adsorb H₂ dissociatively with a surface metal atom to hydrogen atom ratio of 1 [28, 29], the TOF values reflect per surface atom activity, irrespective of their nature or surface concentration. The generated TOF values are reported in Fig. 4e, and the activity increases in order of Co/MgAl₂O₄ (2.3 ± 0.03 s⁻¹) < Co₁Rh₁/MgAl₂O₄ (24.3 ± 0.95 s⁻¹) < Rh/MgAl₂O₄ (40.5 ± 0.74 s⁻¹), suggesting that alloying has promoted the activity of Co surface.

The Arrhenius plots, depicted in Fig. 4f, generate activation energies in the rank of Co/MgAl₂O₄ (107.8 ± 5.3 kJ mol⁻¹) > Co₁Rh₁/MgAl₂O₄ (89.3 ± 3.6 kJ mol⁻¹) > Rh/MgAl₂O₄ (88.1 ± 2.0 kJ mol⁻¹), which coincides with the measured TOF variations. The activation energy for Rh/MgAl₂O₄ is slightly lower than that of Rh/Al₂O₃ (111 kJ mol⁻¹) reported by Iglesia and Wei [50], and the difference is likely due to the effect of support. The activation energy on pristine Co surface is reported to be 148 ± 10 kJ mol⁻¹ on Co/MgO-ZrO₂ catalyst [18], which is different from this work because of both support and promoting effect of Mg.

In short, kinetic studies demonstrate that alloying of Co and Rh, increases the kinetic barrier for methane dissociation and Co-Rh cluster

surface is close to clean and not susceptible to oxidative deactivation. As methane dissociation is the critical step for carbon deposition, one may expect that carbon deposition rate is slowed down on the Co-Rh catalyst. Besides, kinetic data also manifests that the surface activity of Co-Rh cluster is regulatable by changing bulky composition, implying a close to bulk, segregation-free surface composition. In-depth, mechanism based explanation to these kinetic data entails the microkinetic analysis based on DFT calculations.

3.5. DFT calculations and microkinetic analysis

Here, the reaction mechanism has been examined over three representative terrace surfaces of fcc Co, Rh, and Co₁Rh₃ (to represent active surface of Co₁Rh₁/MgAl₂O₄). Fcc cobalt was used because it is the preferred crystal structure of cobalt nanoparticles with diameters below 20 nm [51]. Co(111) [52] and Rh(111) surfaces are the most stable under reforming conditions and thus the predominantly exposed surfaces, and surface segregation free Co₁Rh₃(111) is adopted based on our experimental observations. Table S9 presents all 19 elementary reactions involved in the reaction network of DRM [24,53]. Fig. S21 shows that the two elementary steps, namely, CH₄ dissociation and C* or CH* coupling with O^{*}/OH^{*} are energetically demanding and can therefore be kinetically relevant.

The flux analysis disclosed that CH₄ successive dissociation to CH* (i.e., r₁ to r₃ in Fig. 5) constitutes the main channel over the Co(111), Rh(111) and Co₁Rh₃(111) surfaces, whilst CH* to CO may take routes with varied kinetic contributions. On Co(111) surface, CH* coupling with O^{*} to yield CHO* and its decomposition to CO* (r₅ to r₈, in Fig. 5) is favored (70.65 %) over CH* dehydrogenation to C* (r₄) and its oxidation by either O^{*} (r₆, 28.40 %) or OH^{*} (r₇ and r₉, 0.95 %) to produce CO, thus showing CH* can be readily oxidized before further dehydrogenation, and CH* oxidation is therefore the major channel for CO formation. On Rh(111), however, equivalent contributions from CH* oxidation (r₅ to r₈, 31.44 %) and C* oxidation (r₄, to r₆ or r₇ and r₉, 68.56 %) are deduced. On Co₁Rh₃(111), the contributions of CH* (7.63 %) and C* (91.97 %) oxidation show that C* oxidation is the major channel for CO formation.

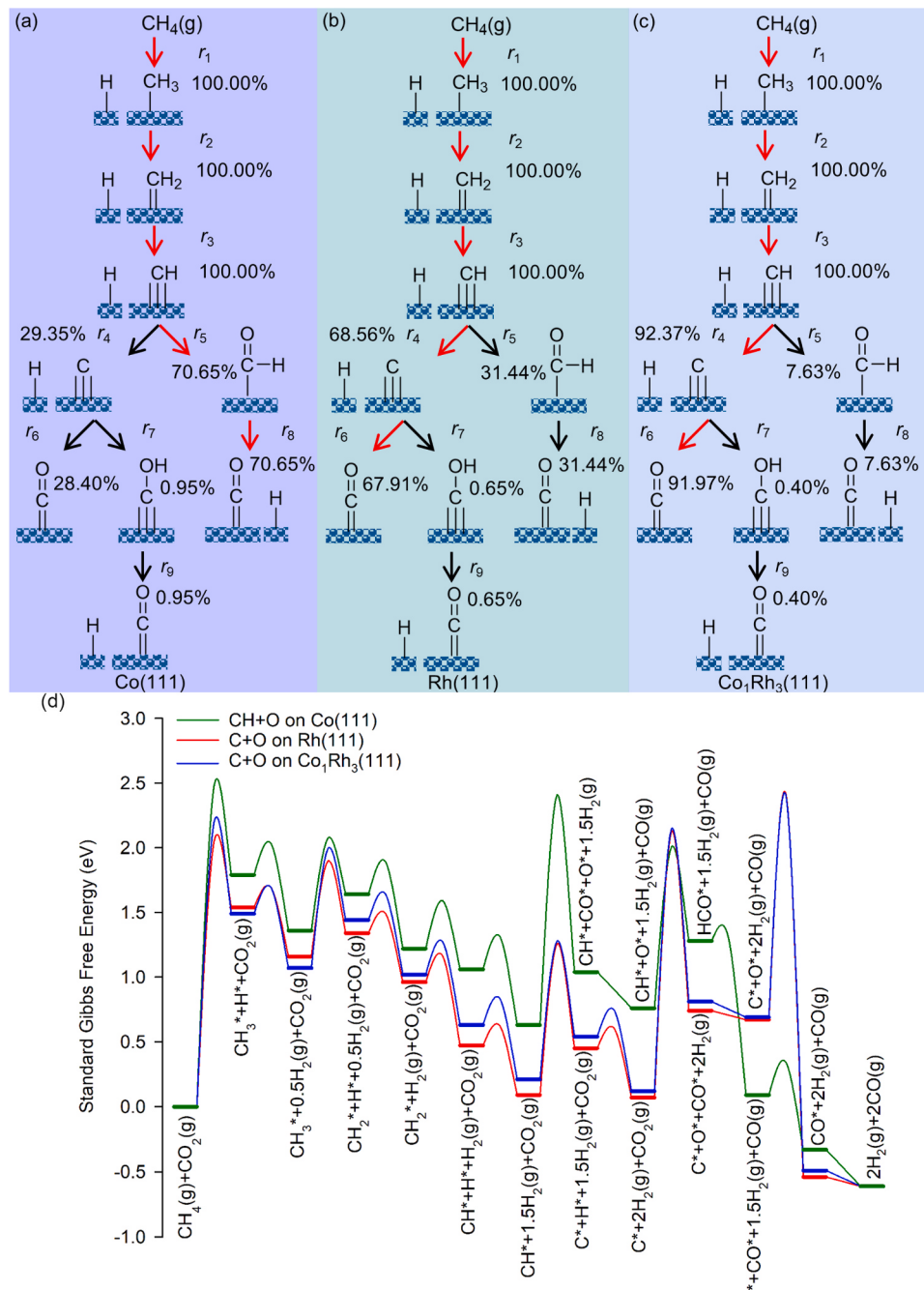


Fig. 5. Flux analysis of DRM under experimental reactor inlet conditions (850 °C, 20 bar of total pressure, with a gas composition of 50 % CH₄, 50 % CO₂, 0 % CO, 0 % H₂, and 0 % H₂O) over (a) Co(111), (b) Rh(111) and (c) Co₁Rh₃(111). The arrows, which are labeled with the percentage of the total reaction flux, show the direction the reversible elementary steps actually proceed. The percentage of the reaction flux was calculated as the absolute value of the net rate for that elementary step divided by the rate for methane consumption. (d) Gibbs free energy diagrams for DRM over Co(111) through CH+O path, Rh(111) and Co₁Rh₃(111) through C+O path at 850 °C.

On Co(111), the rate of the CH^{*}+ O^{*} path is around one order of magnitude higher than that of the C^{*}+ O^{*} path between 720 °C and 850 °C. In contrast, the C^{*}+ O^{*} path can be considered as the dominant reaction pathway on Rh(111) and Co₁Rh₃(111). We plot in Fig. S22(d, e, f) the steady state coverage of dominant surface intermediates against reaction temperature, which have been calculated after thermochemical corrections, in order to consider the influences of reaction temperature and pressure. From Fig. S22 (d-f), it is seen that the nature and concentration of MARIs are less dependent on temperatures, and the MARIs are O^{*} on both Co(111) (0.45 mL) and Co₁Rh₃(111) (0.24 mL) facets, while being C^{*} on Rh(111) (0.31 mL) surface. In addition to the effect of temperature, we plot in Fig. S23 the effect of total pressure on reaction rate and the MARI. The CH + O path is predicted to be the dominant reaction pathway on Co(111) and the C + O path is the dominant reaction pathway on Rh(111) and Co₁Rh₃(111), with the total pressure

ranging from 1 bar to 20 bar. As can be seen from Fig. S23 (d-f), the increase in operation pressure has markedly changed the MARIs on both Co₁Rh₃(111) and Rh(111) surfaces, while no obvious change has been determined on Co(111) surface. On Co(111) facet, the coverage of O^{*} slightly drops from around 0.45–0.41 mL, when the pressure rises from 1 bar to 20 bars. On Rh(111) surface, when the pressure rises from 1 bar to 20 bars, the coverage of C^{*} slightly drops from around 0.31–0.25 mL and the coverage of CH^{*} increases from around 0.08–0.31 mL. In particular, over Co₁Rh₃(111) surface, the coverage of O^{*} drops from 0.24 mL (1 bar) to about 0.12 mL (20 bars), but the coverage of C^{*} increases from 0.01 mL (1 bar) to about 0.14 mL (20 bars). The increase in pressure from ambient to 20 bars has lowered the surface concentration of O^{*}, and simultaneously increased surface C^{*} concentration to an extent close to that of O^{*}, which should favor surface C^{*} oxidation. Correspondingly, the order of the total reaction

rates on the three surfaces, regardless of temperature or pressure, is Co(111) < Co₁Rh₃(111) < Rh(111). The energy barriers are determined to be 117.7, 93.6, 82.0 kJ mol⁻¹ over Co(111), Co₁Rh₃(111) and Rh(111) respectively. Consequently, in the standard Gibbs free energy diagrams (Fig. 5(d)), the Gibbs free energy barriers for the likely rate-determining CH₄ dissociation are determined to be 239.3, 212.3, and 198.8 kJ mol⁻¹ over Co(111), Co₁Rh₃(111) and Rh(111), respectively, providing a rational interpretation of the observed increase in the reaction rate. To help explain the synergistic effect between Co and Rh, the density of states (DOS) projected onto the *d*-states of surface metal atoms on Co₁Rh₃(111) surface was calculated and compared with those on Co(111) and Rh(111), as shown in Fig. S24. Co(111) has a less negative *d*-band center (-1.16 eV) than Rh(111) (-1.71 eV). From Rh(111) to Co₁Rh₃(111), it can be seen that the *d*-band of Rh has been narrowed, leading to an upshift in *d*-band center by about 0.25 eV. However, the *d*-band center of Co is shifted downward by 0.13 eV from Co(111) to Co₁Rh₃(111). The *d*-band centers scale with the activation barriers for methane dissociation on the catalyst surfaces (Fig. S25), which agrees well with the activation barriers derived from kinetic studies.

To correlate the DFT derived kinetics to the experimental data, the logarithm to base *e* of TOFs as a function of the reciprocal of temperature (i.e., Arrhenius plot of ln(TOF) versus 1/T) are reported in Fig. S26. The estimated apparent activation energies on Co(111), Co₁Rh₃(111) and Rh(111) are, respectively, 125.0, 102.6 and 93.9 kJ mol⁻¹ at temperatures between 710 °C and 730 °C and ambient pressure, viz. the conditions relevant to the kinetic data measurements. The measured activation energies follow an incremental order: Co(111) < Co₁Rh₃(111) < Rh(111), which qualitatively agrees with the experimental data (Fig. 4). The theoretically derived data are perceived to be generally larger than these experimentally derived ones, and the discrepancy could be accounted for by taking into consideration that only the most stable fcc (111) terrace sites have been considered here, whereas under-

coordinated sites could contribute to the lowered activation energies. Table S11 shows the predicted reaction orders on Co(111), Rh(111), and Co₁Rh₃(111) at 720 °C. It is apparent that the reaction rate increases linearly with increasing CH₄ partial pressure, but is impervious to partial pressures of CO₂, CO, H₂ and H₂O.

Furthermore, to understand the impact of alloying on C* nucleation and refractory carbon formation, the stability of graphene layer on the catalyst surfaces has been assessed theoretically, following a method established by Bengaard et al [11]. (Fig. S27). Surface C*(often denoted as C₀) [10] derived from CH₄ dissociation and successive dehydrogenation can be coupled with neighboring ones to form C-C bonds and changed to C_β. Nucleation and further growth of the C_β produces graphene-like, encapsulating carbon, which may undergo diffusion along carbon/metal interface to generate whisker carbon (Scheme 1) [9]. A strong stabilization energy of graphene layer by metal surface would suggest a high possibility of C* nucleation.

We have estimated the critical size of graphene layers over Co(111), Rh(111) and Co₁Rh₃(111), as illustrated in Fig. 6. A critical graphene island size on Co(111) was 21 atoms, much smaller than 3045 atoms over Rh(111), which explains why soft carbon was present on the spent Rh catalyst surface. Experimentally, graphene growth on Rh(111) surface [54] and *hcp*-structured Co(0001) surface [12] (with identical surface Co atom alignment to that of *fcc* Co(111) surface) have been observed by Scanning Tunneling Microscopy, thus confirming the predicted stability for large graphene layers on these surfaces. Intriguingly, no stable graphene island could be obtained on Co₁Rh₃(111) surface, meaning that nucleation of carbon is energetically unfavorable. The hindrance of surface carbon nucleation and transformation into refractory carbons suggest that reactive carbonaceous intermediates, which could be facilely gasified by coupling with O*, are the major type of coke formed on the Co-Rh alloy surface. This destabilization effect can be rationalized in terms of combined electronic and geometrical effects

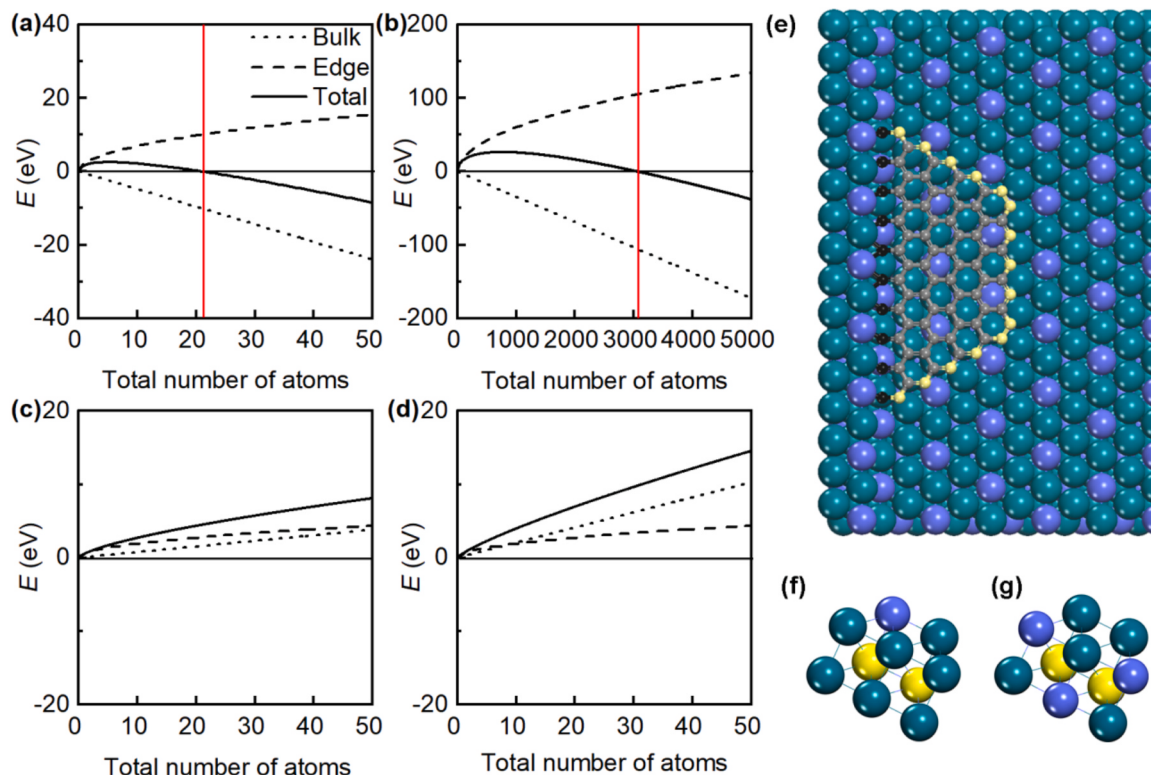


Fig. 6. The total energy (*E*) of a graphene island, the edge and bulk energies on Co(a), Rh(b) and Co₁Rh₃(c, d) as a function of number of C atoms *N*_{tot}. The dotted lines are bulk energy, the dashed lines are the edge energy, and the full lines are the total energy of the island. The red line indicates the critical island size. The model of graphene island is semi-hexagonal and attached to a step edge (e). There are two atomic arrangements of adsorbed C* atoms on Co₁Rh₃(211) surface, which are named (f) Co₁Rh₃(211)_a and (g) Co₁Rh₃(211)_b, corresponding to energy scenarios of (c) and (d), respectively.

[11].

4. Conclusions

In summary, we demonstrate that Co-Rh/MgAl₂O₄ is a stable methane dry reforming catalyst at harsh operation condition of 850 °C and 20 bars. Surface segregation free Co₁Rh₃ intermetallic clusters have been determined as the active phase possessing outstanding coke-resistant property, as disclosed by comprehensive characterizations and control experiments. The Co₁Rh₃ intermetallic clusters show long term stability and no refractory, whisker carbon has been observed on the catalyst surface after 100 h TOS test. Kinetic studies demonstrates that the reaction proceeds mainly through C* surface oxidation by O* over Co₁Rh₃(111) surface, instead of CH* oxidation that dominates on Co(111) surface. The kinetic law can be well correlated to the DFT calculations with respect to reaction orders and activation energies. Combined microkinetic and experimental studies disclose the underlying reasons responsible for the outstanding coke-resistance to be: (1) reduced and balanced C* and O* intermediate coverages that avoid surface C* accumulation dynamically, (2) suppressed nucleation of surface carbon atoms to afford refractory carbon that is resistant to CO₂ oxidation, (3) alleviated surface oxidative deactivation under pressurized conditions and by H₂ spillover brought about by Rh.

The kinetic features can be well correlated to the *d*-band electronic structure of metal clusters, thus suggesting that the surface C* deposition and gasification are mainly determined by the electronic structure of catalyst. Meanwhile, the formation of graphene island, a key step for surface C* atom nucleation and formation of refractory whisker carbon, is governed by the geometric features of catalyst surface. Only when the critical size of graphene island is extended virtually to infinite, i.e., no stable graphene can form over a catalyst surface, could the nucleation of C* be suppressed. As soft carbon species can be readily oxidized by O*, the merely formation of such surface intermediates would promote the stability of a working catalyst. Our results therefore highlight that suppression of surface carbon atom nucleation should be considered as a key factor for stable catalyst design. These insights on the electronic structure of Co₁Rh₃ also offer a guide for stable reforming catalyst design and may also have implications for carbon growth. In future studies, it is desirable to identify even low-cost catalysts with alike electronic and geometric properties for the operation of DRM under pressurized conditions.

CRediT authorship contribution statement

Qing Liu carried out most of experiments (catalyst preparation, catalytic assessments, kinetic studies and most of characterizations), data curation, wrote-original draft. Yang Liu performed XPS measurement and analysis. Ning Zhou conducted DFT calculations and assisted in preparation of the manuscript. Penghao Zhang carried out kinetic studies experimentally. Zhicheng Liu supervised and assisted characterizations. Evgeny I. Vovk supervised XPS measurement and analysis. Yi-An Zhu worked out the kinetic rules for the reaction, funding acquisition, resources, writing-review & editing. Yong Yang supervised the XPS *in situ* studies, funding acquisition, resources, writing-review & editing. Kake Zhu supervised and designed the research plan, funding acquisition, project administration, writing-review & editing.

Declaration of Competing Interest

We declare that we do not have any commercial or associative interest that represents a conflict of interest in connection with the work submitted.

Data availability

Data will be made available on request.

Acknowledgments

Authors are grateful for the financial support from the National Natural Science Foundation of China (No. 22178111, 22073027, 92045301, 22072107, 22072092). YY and EV would like to thank Ministry of Science and Technology (2022YFA1503802).

Appendix A. Supporting information

Supplementary data associated with this article can be found in the online version at doi:10.1016/j.apcatb.2023.123102.

References

- [1] P.M. Mortensen, I. Dybkjær, *Appl. Catal., A* 495 (2015) 141–151.
- [2] K. Raghuvanshi, C. Zhu, M. Ramezani, S. Menegatti, E.E. Santiso, D. Mason, J. Rodgers, M.E. Janka, M. Abolhasani, *ACS Catal.* 10 (2020) 7535–7542.
- [3] I.V. Yentekakis, P. Panagiotopoulou, G. Artemakis, *Appl. Catal., B* 296 (2021), 120210.
- [4] L.A. Schulz, L.C.S. Kahle, K.H. Delgado, S.A. Schunk, A. Jentys, O. Deutschmann, J. A. Lercher, *Appl. Catal., A* 504 (2015) 599–607.
- [5] J. Wei, E. Iglesias, *J. Catal.* 224 (2004) 370–383.
- [6] L.C.S. Kahle, T. Roussiére, L. Maier, K. Herrera Delgado, G. Wasserschaff, S. A. Schunk, O. Deutschmann, *Ind. Eng. Chem. Res.* 52 (2013) 11920–11930.
- [7] S.C. Teunier, P. Neumann, F.V. Linde, *Oil Gas. Eur. Mag.* 27 (2001) 44–46.
- [8] A. Ramirez, K. Lee, A. Harale, L. Gevers, S. Telalovic, B. Al Solami, J. Gascon, *ChemCatChem* 12 (2020) 5919–5925.
- [9] S. Helveg, C. López-Cartes, J. Sehested, P.L. Hansen, B.S. Clausen, J.R. Rostrup-Nielsen, F. Abild-Pedersen, J.K. Nørskov, *Nature* 427 (2004) 426–429.
- [10] M. Torimoto, Y. Sekine, *Catal. Sci. Technol.* 12 (2022) 3387–3411.
- [11] H.S. Bengaard, J.K. Nørskov, J. Sehested, B.S. Clausen, L.P. Nielsen, A. Molenbroek, J.R. Rostrup-Nielsen, *J. Catal.* 209 (2002) 365–384.
- [12] C.J. Weststrate, A.C. Kizilkaya, E.T.R. Rossen, M.W.G.M. Verhoeven, I.M. Ciobăcă, A.M. Saib, J.W. Niemantsverdriet, *J. Phys. Chem. C* 116 (2012) 11575–11583.
- [13] J.R. Rostrup-Nielsen, *J. Catal.* 85 (1984) 31–43.
- [14] F. Besenbacher, I. Chorkendorff, B.S. Clausen, B. Hammer, A.M. Molenbroek, J. K. Nørskov, I. Stensgaard, *Science* 279 (1998) 1913–1915.
- [15] S. Chen, J. Zaffran, B. Yang, *ACS Catal.* 10 (2020) 3074–3083.
- [16] A.H. Dam, H. Wang, R. Dehghan-Niri, X. Yu, J.C. Walmsley, A. Holmen, J. Yang, D. Chen, *ChemCatChem* 11 (2019) 3401–3412.
- [17] S. Joo, K. Kim, O. Kwon, J. Oh, H.J. Kim, L. Zhang, J. Zhou, J.-Q. Wang, H. Y. Jeong, J.W. Han, G. Kim, *Angew. Chem. Int. Ed.* 60 (2021) 15912–15919.
- [18] W. Tu, M. Ghoussooub, C.V. Singh, Y.C. Chin, *J. Am. Chem. Soc.* 139 (2017) 6928–6945.
- [19] H. Wang, N.V. Srinath, H. Poelman, C. Detavernier, P. Li, G.B. Marin, V.V. Galvita, *Catal. Sci. Technol.* 10 (2020) 6987–7001.
- [20] A.W. Budiman, S.-H. Song, T.-S. Chang, C.-H. Shin, M.-J. Choi, *Catal. Surv. Asia* 16 (2012) 183–197.
- [21] Y.J. Wong, M.K. Koh, N.F. Khairudin, S. Ichikawa, Y. Morikawa, A.R. Mohamed, *ChemCatChem* 11 (2019) 5593–5605.
- [22] G. Jones, J. Jakobsen, S. Shim, J. Kleis, M. Andersson, J. Rossmeisl, F. Abildpedersen, T. Bligaard, S. Helveg, B. Hinemann, *J. Catal.* 259 (2008) 147–160.
- [23] P. van Helden, I.M. Ciobăcă, R.J.L. Coetzer, *Catal. Today* 261 (2016) 48–59.
- [24] Y. Yu, J. Yang, K. Zhu, Z. Sui, D. Chen, Y.-A. Zhu, X. Zhou, *ACS Catal.* 11 (2021) 8881–8894.
- [25] Y. Wong, H.H. Halim, N.F. Khairudin, T.N. Pham, S.E.M. Putra, Y. Hamamoto, K. Inagaki, I. Hamada, A.R. Mohamed, Y. Morikawa, *J. Phys. Chem. C* 125 (2021) 21902–21913.
- [26] J.L. Rogers, M.C. Mangarella, A.D. D'Amico, J.R. Gallagher, M.R. Dutzer, E. Stavitski, J.T. Miller, C. Sievers, *ACS Catal.* 6 (2016) 5873–5886.
- [27] A. Jiang, J. Chen, S. Liu, Z. Wang, Q. Li, D. Xia, M. Dong, *ACS Appl. Nano Mater.* 4 (2021) 13716–13723.
- [28] J. Saavedra Lopez, V. Le Barbier Dagle, C.A. Deshmane, L. Kovarik, R.S. Wegeng, R. A. Dagle, *Catalysts* 9 (2019) 801.
- [29] P. Djinović, A. Pintar, *Appl. Catal., B* 206 (2017) 675–682.
- [30] Z. Liu, F. Gao, Y.-A. Zhu, Z. Liu, K. Zhu, X. Zhou, *Chem. Commun.* 56 (2020) 13536–13539.
- [31] T. Zhang, Z. Liu, Y.-A. Zhu, Z. Liu, Z. Sui, K. Zhu, X. Zhou, *Appl. Catal., B* 264 (2020), 118497.
- [32] G. Kresse, J. Furthmüller, *Phys. Rev. B* 54 (1996) 11169–11186.
- [33] J. Wellendorff, K.T. Lundgaard, A. Mogelhøj, V. Petzold, D.D. Landis, J.K. Nørskov, T. Bligaard, K.W. Jacobsen, *Phys. Rev. B: Condens. Matter Mater. Phys.* 85 (2012), 235149.
- [34] P.E. Blöchl, *Phys. Rev. B* 50 (1994) 17953–17979.
- [35] H.J. Monkhorst, J.D. Pack, *Phys. Rev. B* 13 (1976) 5188–5192.
- [36] M. Methfessel, A.T. Paxton, *Phys. Rev. B* 40 (1989) 3616–3621.
- [37] D. Sheppard, R. Terrell, G. Henkelman, *J. Chem. Phys.* 128 (2008), 134106.
- [38] A.J. Medford, C. Shi, M.J. Hoffmann, A.C. Lausche, S.R. Fitzgibbon, T. Bligaard, J. K. Nørskov, *Catal. Lett.* 145 (2015) 794–807.
- [39] P.J. Linstrom, W.G. Mallard, *J. Chem. Eng. Data* 46 (2001) 1059–1063.
- [40] S.R. Bahn, K.W. Jacobsen, *Comput. Sci. Eng.* 4 (2002) 56–66.

[41] L. Xiao, F. Ma, Y.-A. Zhu, Z.-J. Sui, J.-H. Zhou, X.-G. Zhou, D. Chen, W.-K. Yuan, *Chem. Eng. J.* 377 (2019), 120049.

[42] A. Yu, S.Y. Kim, C. Lee, M.H. Kim, Y. Lee, *ACS Appl. Mater. Interfaces* 11 (2019) 46886–46893.

[43] R. Riva, H. Miessner, R. Vitali, G. Del Piero, *Appl. Catal., A* 196 (2000) 111–123.

[44] Z. Zsoldos, L. Guczi, *J. Phys. Chem.* 96 (1992) 9393–9400.

[45] M.A. Ali, T. Kimura, Y. Suzuki, M.A. Al-Saleh, H. Hamid, T. Inui, *Appl. Catal., A* 227 (2002) 63–72.

[46] G.A. Somorjai, Y. Li. *Introduction to Surface Chemistry and Catalysis*, 2nd edition, John Wiley & Sons, Inc, 2010, pp. 297–301.

[47] F. Zhang, Z. Liu, S. Zhang, N. Akter, R.M. Palomino, D. Vovchok, I. Orozco, D. Salazar, J.A. Rodriguez, J. Llorca, J. Lee, D. Kim, W. Xu, A.I. Frenkel, Y. Li, T. Kim, S.D. Senanayake, *ACS Catal.* 8 (2018) 3550–3560.

[48] S.L. Leung, J. Wei, W.L. Holstein, M. Avalos-Borja, E. Iglesia, *J. Phys. Chem. C* 124 (2020) 20143–20160.

[49] S.A. Theofanidis, R. Batchu, V.V. Galvita, H. Poelman, G.B. Marin, *Appl. Catal., B* 185 (2016) 42–55.

[50] J. Wei, E. Iglesia, *J. Catal.* 225 (2004) 116–127.

[51] O. Kitakami, H. Sato, Y. Shimada, F. Sato, M. Tanaka, *Phys. Rev. B* 56 (1997) 13849–13854.

[52] S. Chen, J. Zaffran, B. Yang, *Appl. Catal., B* 270 (2020), 118859.

[53] Y.-A. Zhu, D. Chen, X. Zhou, W. Yuan, *Catal. Today* 148 (2009) 260–267.

[54] G. Dong, J.W. Frenken, *ACS Nano* 7 (2013) 7028–7033.